Spin correlations in $Ca_3Co_2O_6$: Polarized-neutron diffraction and Monte Carlo study

Joseph A. M. Paddison,[1,2] Stefano Agrestini,[3] Martin R. Lees,[4] Catherine L. Fleck,[4] Pascale P. Deen,[5,6] Andrew L. Goodwin,[1] J. Ross Stewart,[2] and Oleg A. Petrenko[4,*]

[1]*Department of Chemistry, University of Oxford, Inorganic Chemistry Laboratory, South Parks Road, Oxford OX1 3QR, United Kingdom*
[2]*ISIS Facility, Rutherford Appleton Laboratory, Chilton, Didcot, Oxfordshire OX11 0QX, United Kingdom*
[3]*Max Planck Institute for Chemical Physics of Solids, Nöthnitzerstr. 40, 01187 Dresden, Germany*
[4]*Department of Physics, University of Warwick, Coventry, CV4 7AL, United Kingdom*
[5]*Institut Laue-Langevin, 6 rue Jules Horowitz, 38042 Grenoble, France*
[6]*European Spallation Source, ESS AB, SE-22100 Lund, Sweden*

(Received 13 December 2013; revised manuscript received 12 May 2014; published 11 July 2014)

We present polarized-neutron diffraction measurements of the Ising-type spin-chain compound $Ca_3Co_2O_6$ above and below the magnetic ordering temperature T_N. Below T_N, a clear evolution from a pure spin-density wave (SDW) structure to a mixture of SDW and commensurate antiferromagnet (CAFM) structures is observed on cooling. For a rapidly cooled sample, the majority phase at low temperature is the SDW, while if the cooling is performed sufficiently slowly, then the SDW and the CAFM structure coexist between 1.5 and 10 K. Above T_N, we use Monte Carlo methods to analyze the magnetic diffuse scattering data. We show that both intrachain and interchain correlations persist above T_N, but are essentially decoupled. Intrachain correlations resemble the one-dimensional ferromagnetic Ising model, while interchain correlations resemble the frustrated triangular-lattice antiferromagnet. Using previously published bulk property measurements and our neutron diffraction data, we obtain values of the ferromagnetic and antiferromagnetic exchange interactions and the single-ion anisotropy.

DOI: 10.1103/PhysRevB.90.014411 PACS number(s): 75.25.−j, 75.30.Fv, 75.50.Ee

I. INTRODUCTION

The spin-chain compound $Ca_3Co_2O_6$ offers a rare opportunity to investigate the interplay of frustration and low dimensionality in a triangular lattice of Ising chains. Some of the most interesting observations of $Ca_3Co_2O_6$ have been made in an applied magnetic field, where the appearance of magnetization plateaus [1] at low temperature has been linked to a quantum tunneling mechanism [2]. However, even in zero field $Ca_3Co_2O_6$ demonstrates very complex and unexpected behavior. Below $T_N = 25$ K, $Ca_3Co_2O_6$ undergoes an unusual order-order transition, an ultraslow magnetic relaxation, and a coexistence of several magnetic phases [3], while above T_N the persistence of dispersive spin-wave excitations indicates that strong spin correlations remain present [4]. A substantial and prolonged theoretical interest in this compound [5–9] is thus not unexpected (see Ref. [10] for a recent review).

The crystal structure of $Ca_3Co_2O_6$ is rhombohedral (space group $R\bar{3}c$) and consists of chains made up of alternating face-sharing octahedral (Co_I^{3+}; $S = 0$) and trigonal prismatic (Co_{II}^{3+}; $S = 2$) CoO_6 polyhedra [11,12]. The chains are directed along the c axis and are arranged on a triangular lattice in the ab plane. The trigonal crystal field and spin-orbit coupling generate an Ising-type magnetic anisotropy at the Co_{II}^{3+} site, with the easy axis parallel to the chains [5,13]. Spins are coupled by ferromagnetic (FM) interactions within the chains, while much weaker antiferromagnetic (AFM) interactions couple adjacent chains along helical pathways [14,15]. Below T_N, a magnetic order is stabilized in the form of a longitudinal amplitude-modulated spin-density wave (SDW) propagating along the c axis with a periodicity of about 1000 Å. There is a phase shift of 120° in the modulation between adjacent chains [16–18]. Recent powder neutron diffraction results [3] revealed an order-order transition from the SDW structure to a commensurate antiferromagnetic (CAFM) phase. This transition occurs over a time scale of several hours and is never complete.

Despite longstanding interest in $Ca_3Co_2O_6$, a detailed understanding of zero-field spin correlations as a function of temperature has not yet been achieved. Here, we attempt to address three outstanding questions: (i) What is the temperature dependence of the fractions of SDW and CAFM phases below T_N? (ii) What is the nature of the spin correlations in the paramagnetic phase above T_N, and how are these correlations related to reported anomalies in thermodynamic (bulk) measurements [2,19–21]? (iii) Can the temperature-dependent behavior of $Ca_3Co_2O_6$ be explained in a consistent way using an effective spin Hamiltonian?

To address these questions, we have performed polarized-neutron scattering measurements on a polycrystalline sample of $Ca_3Co_2O_6$ above and below T_N. We employ Monte Carlo methods to interpret our data above T_N and to calculate thermodynamic quantities. Our paper is structured as follows. Details of our experiments and analysis methods are given in Sec. II. In Sec. III A, we address the effect of temperature and sample cooling rate on the coexistence of magnetic phases below T_N. In Sec. III B, we use Monte Carlo methods to extract the spin correlation functions along and between the chains above T_N. Finally, in Sec. IV we develop a model of the magnetic interactions which is compatible both with our neutron data and with previously reported measurements of thermodynamic properties [2,20,21].

*o.petrenko@warwick.ac.uk

II. EXPERIMENTAL AND TECHNICAL DETAILS

A polycrystalline sample of $Ca_3Co_2O_6$ of mass 3.6 g was synthesized via a solid-state method [13,22,23]. The magnetic properties of the sample were checked by magnetization measurements and agree with those reported previously [13,21–24].

We performed polarized-neutron diffraction experiments using the D7 instrument at the ILL in Grenoble, France. D7 is a cold-neutron diffuse scattering spectrometer equipped with xyz polarization analysis [25], which uses 132 ^{3}He detectors to cover a scattering range of about 140°. We used neutrons monochromated to wavelengths of 4.8 and 3.1 Å, allowing the scattering to be measured in the range $0.34 < q < 2.48$ Å^{-1} and $0.53 < q < 3.46$ Å^{-1}, respectively. In order to avoid possible complications from the influence of the out-of-plane components to forward scattering [26], the data for scattering angles less than 20° have been ignored in the refinements.

Standard data analysis techniques (which included detector efficiency normalization from vanadium standards and polarization efficiency calculations from an amorphous silica standard) were used to calculate the magnetic, nuclear, and spin-incoherent scattering components from the initial data. The diffraction data obtained below T_N were refined using the FULLPROF program [27]. D7 is also equipped with a Fermi chopper, which permits inelastic scattering measurements with a resolution of 3% of the incident energy, thereby giving the ability to differentiate between elastic and inelastic contributions [25]. All attempts to detect an inelastic signal at any temperature were unsuccessful; therefore, within D7's resolution of about 0.15 meV, the signal should be presumed to be totally elastic.

We refined the magnetic diffuse scattering patterns obtained above T_N using the SPINVERT program [28], which implements a reverse Monte Carlo (RMC) algorithm [29,30]. In the RMC refinements, a supercell of the crystallographic unit cell is first generated, a classical Ising spin with random orientation (up/down) is assigned to each Co_{II}^{3+} site, and the sum of squared residuals is calculated:

$$\chi^2 = W \sum_q \left[\frac{s I_{\rm calc}(q) - I_{\rm expt}(q)}{\sigma(q)} \right]^2, \qquad (1)$$

in which $I(q)$ denotes a powder-averaged magnetic scattering intensity, subscripts "calc" and "expt" denote calculated and experimental values, $\sigma(q)$ is an experimental uncertainty, W is an empirical weighting factor, and s is a refined overall scale factor. A randomly chosen spin is then flipped, the change in χ^2 is calculated, and the proposed spin flip is accepted or rejected according to the METROPOLIS algorithm. This process is repeated until no further reduction in χ^2 is observed. The scattering pattern is calculated from the spin configuration using the general expression of Ref. [31] which takes magnetic anisotropy into account. In our refinements, we used periodic spin configurations of size $12 \times 7 \times 11$ orthorhombic unit cells ($N = 11\,088$ spins), which represented a compromise between maximizing the simulation size and keeping the computer time required within reasonable limits. Refinements were performed for 100 proposed flips per spin, and all calculated quantities were averaged over 10 independent spin configurations in order to minimize the statistical noise.

We performed direct Monte Carlo (DMC) simulations using the classical Ising Hamiltonian

$$H = -\frac{1}{2} \sum_{i,j} J_{ij} S_i^z S_j^z, \qquad (2)$$

in which the z component of spin $S^z = \pm S$, where $S = 2$ is the spin length, and the transverse couplings are neglected (i.e., $S_i^x S_j^x = S_i^y S_j^y = 0$). We also considered the anisotropic Hamiltonian

$$H = -\frac{1}{2} \sum_{i,j} J_{ij} S_i^z S_j^z - D \sum_i \left(S_i^z\right)^2, \qquad (3)$$

in which the transverse coupling terms are again neglected and S_i^z can take now five values: $S_i^z = \pm 2, \pm 1, 0$. For $T \ll DS^2$, only the $S^z = \pm 2$ states are occupied, and Eq. (3) is equivalent to Eq. (2). We finally investigated the classical anisotropic Heisenberg Hamiltonian

$$H = -\frac{1}{2} \sum_{i,j} J_{ij} \mathbf{S}_i \cdot \mathbf{S}_j - D \sum_i \left(S_i^z\right)^2, \qquad (4)$$

in which the $\mathbf{S}_i$ are three-component vectors having length S and z component S_i^z. In all models, J_{ij} is a general interaction between pairs of spins i, j, D is a single-ion anisotropy term, and the factor of $\frac{1}{2}$ corrects for the double counting of pairwise interactions. In Sec. III B, we consider specifically interactions between nearest-neighbor and third-neighbor spins, which we label J_1 and J_3, respectively.

Direct Monte Carlo simulations were performed using a simulated annealing algorithm in which a periodic spin configuration was initialized with random spin orientations and slowly cooled. The initial temperature was $T = 15 J_1 S^2$ for the Ising model and $T = 60 J_1 S^2$ for the anisotropic models, and ratio of adjacent temperatures was equal to 0.96. At each temperature, 10^4 moves per spin were proposed for equilibration, followed by at least 10^5 proposed moves for calculations of the bulk properties. For the Ising model, a proposed spin move involved choosing a spin at random and flipping its orientation. For the five-state model, a proposed spin move involved choosing one of the five possible states at random. For the anisotropic Heisenberg model, two kinds of move were alternated: randomly choosing a new spin orientation on the surface of a sphere, and a simple spin flip ($\mathbf{S}_i \rightarrow -\mathbf{S}_i$), where the latter is used to allow the simulation to move rapidly between Ising-type states at low T [32]. Each proposed spin move was accepted or rejected according to the METROPOLIS algorithm. To simulate diffraction patterns, we used five independent spin configurations, each of size $18 \times 10 \times 16$ orthorhombic unit cells ($N = 34\,560$ spins); an approximately cubic supercell was used because calculating powder diffraction patterns involves spherically averaging spin correlation functions in real space [31]. For bulk-properties calculations, we used a spin configuration of size of $5 \times 3 \times 64$ orthorhombic unit cells ($N = 11\,520$ spins); these dimensions were chosen since the correlation length along c is longer than in the ab plane (Sec. III B). The magnetic susceptibility per spin χ and heat capacity per spin $C_{\rm mag}$ were calculated from

the fluctuation-dissipation relations

$$\chi T = \frac{1}{N}\left(\langle M_z^2\rangle - \langle M_z\rangle^2\right), \quad (5)$$

$$C_{\mathrm{mag}} = \frac{1}{NT^2}(\langle E^2\rangle - \langle E\rangle^2), \quad (6)$$

where $M_z = \sum_i S_i^z/S$ is the total magnetization (normalized by spin length), $E = \sum_i E_i$ the total energy, and angle brackets denote the time average. For comparison with experimental data, χT is converted into units of $\mathrm{K\,m^3\,mol^{-1}}$ by multiplying by $N_A\mu_0\mu_{\mathrm{eff}}^2 k_B^{-1}$, with the effective magnetic moment $\mu_{\mathrm{eff}} = (2S^z + L^z)\mu_B$, and C_{mag} is converted into $\mathrm{J\,K^{-1}\,mol^{-1}}$ by multiplying by $N_A k_B$.

III. RESULTS AND DISCUSSION

A. Low-temperature data

The CAFM phase detected previously in $Ca_3Co_2O_6$ has been proven to be metastable in nature [3]. Given this, we have experimented using two different protocols for cooling the sample, denoted *slow cooling* and *rapid cooling*. For the slow cooling, the sample was initially cooled to 30 K; the temperature was then reduced down to 5 K in steps of 5 K, and finally to the base temperature of 1.5 K. Diffraction patterns were recorded at each temperature step with a data collection time of 4 to 5 h; therefore, the total cooling time to base temperature was more than 24 h. For the rapid cooling, the sample was quickly (within a few minutes) cooled from just above the ordering temperature ($\sim$ 25 K) down to the base temperature of the cryostat and equilibrated for 15 min. The measurement time at the base temperature was 4 h. The sample was then warmed up to 5, 7.5, 10 and 15 K with 4-h-long measurements at each temperature. The neutron diffraction patterns recorded with 4.8-Å neutrons following these two protocols are shown in Figs. 1(a) and 1(b), respectively.

The most intense magnetic Bragg peaks corresponding to the SDW and CAFM phases appear at 0.79 and 0.69 $\mathrm{Å^{-1}}$, respectively. The presence of these two magnetic phases can therefore be easily followed in Fig. 1.

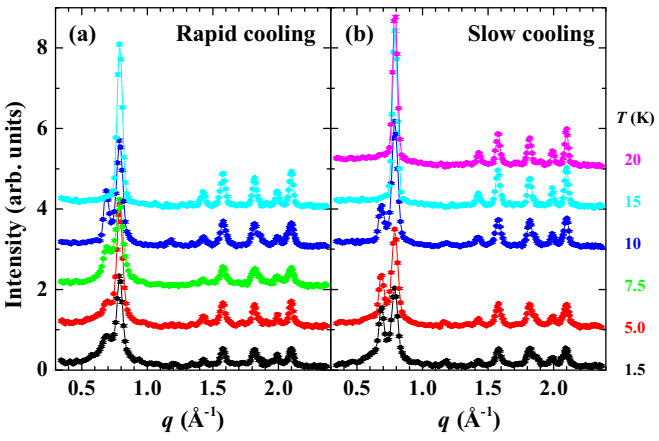

FIG. 1. (Color online) Magnetic powder neutron diffraction intensity profiles of $Ca_3Co_2O_6$ measured with 4.8-Å neutrons on warming after rapid cooling (a) and on slow cooling (b). The curves are offset for clarity.

The SDW phase is the majority phase at all temperatures. The CAFM phase is present at temperatures below and including 10 K, but for the rapid cooling protocol it is barely visible at lower temperatures (1.5 and 5 K). On the other hand, for the slow cooling protocol intense and narrow magnetic reflections from the CAFM phase can be observed even at the lowest temperatures. These results provide evidence that the extremely slow dynamics existing below 10 K hamper the development of the long-range CAFM phase in the case of a fast cooling procedure. Apart from the long-range SDW and CAFM phases, a short-range magnetic component is clearly present at $T < 15$ K for both cooling protocols, in agreement with the previous unpolarized neutron diffraction data [3,16] and a recent magnetocaloric study [33]. In the refinement, it is rather difficult to distinguish this short-range component from a background signal that varies slightly as function of scattering angle. Figures 2(a) and 2(b) illustrate this point by showing the refinement of the $T = 5.0$ K data for rapid and slow cooling regimes using both flat and variable backgrounds.

The actual numbers for the phase fraction of the short-range component vary considerably depending on the presumed shape of the background. The temperature dependence of the magnetic fractions are shown in Figs. 2(c) and 2(d) for both cooling regimes.

The slow cooling procedure results in the simultaneous presence of both magnetic long-range-ordered phases at low temperature (from 1.5 to 10 K), while at higher temperatures (at 15 and 20 K) only the SDW phase is visible. In contrast to the rapid cooling data, for the slow cooling procedure the fraction of the CAFM phase does not show a maximum around 10 K but monotonically increases, at the expense of the SDW phase, as the temperature is further reduced. This result shows that the particular protocol used for cooling the sample strongly affects the evolution of the order-order transition between the SDW and CAFM phases. This observation is an effect of the rapid increase of the characteristic time of the transition process between the SDW and CAFM phases as the temperature is decreased [3]. The dependence on the cooling procedure shown by ac susceptibility measurements [24] is probably related to the particular dynamics of the long-range magnetic order in $Ca_3Co_2O_6$.

Further systematic measurements would be required to investigate whether the presence of the maximum found at about 10 K in the temperature dependence of the CAFM fraction for the rapid cooling protocol is correlated with the amount of time the sample is kept at low temperatures. These measurements (not attempted here) would be better suited for an unpolarized neutron high-intensity diffractometer capable of much faster data collection rates.

Due to the relatively low q-resolution of the D7 diffractometer, it was not possible to detect a small ($\sim$ 0.01 $\mathrm{Å^{-1}}$) [16,17] incommensuration in the magnetic reflections associated with the long-period modulation of the SDW magnetic structure along the c axis.

Additional data were collected using the slow cooling protocol with 3.1-Å neutrons. The higher-energy incident neutrons allowed for diffraction up to a higher maximum q,

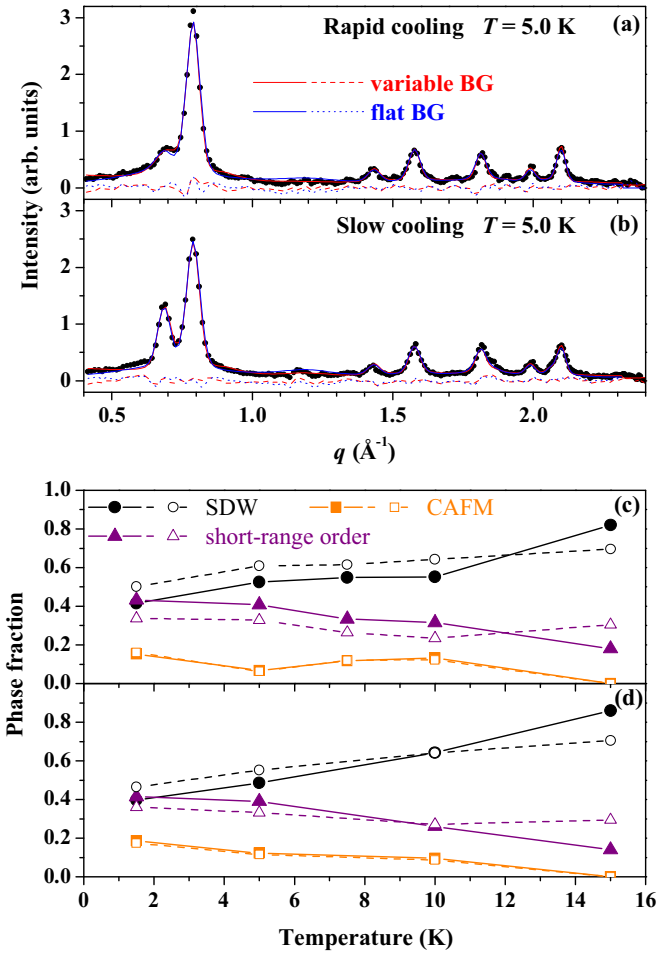

FIG. 2. (Color online) Top panels: Magnetic component of powder neutron diffraction patterns of $Ca_3Co_2O_6$ collected at 5.0 K (a) on warming to this temperature after rapid cooling to 1.5 K and (b) on slow cooling to this temperature. Dots represent the experimental data, while the lines show the calculated patterns and difference curves. Bottom panels: Temperature dependence of the fractions of the SDW, CAFM, and short-range order phases for (c) rapid cooling and (d) slow cooling protocols. Solid (open) symbols correspond to the refinement which includes (excludes) a variable background.

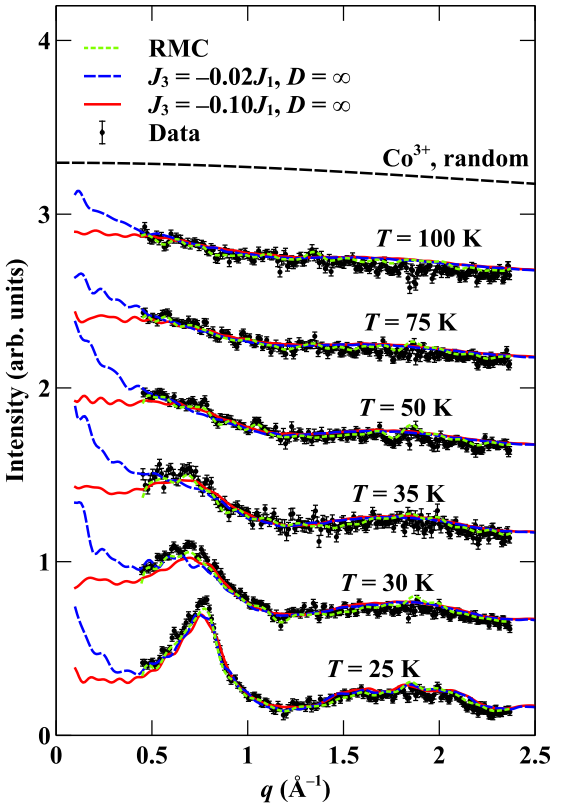

FIG. 3. (Color online) Magnetic diffuse scattering patterns from $Ca_3Co_2O_6$ at six temperatures above T_N. Filled black symbols represent experimental data. The dotted green lines show reverse Monte Carlo fits (see main text for details). The solid red lines are calculated using direct Monte Carlo simulations of the Ising model with exchange interactions $J_3/J_1 = -0.10$ ($J_1S^2 = 22.9$ K), and the dashed blue lines for $J_3/J_1 = -0.02$ ($J_1S^2 = 36.8$ K). The curves for different temperatures are consecutively offset by 0.5 units for clarity. The paramagnetic squared form factor for Co^{3+} (adjusted by the overall intensity scale determined from RMC refinement) is shown as a dashed black line for comparison.

but the data collected essentially followed the same trend as in Fig. 1(b) and are therefore not shown here.

B. High-temperature data

High-temperature magnetic diffuse scattering data were collected at six temperatures above T_N and are shown in Fig. 3. No appreciable dependence of the scattering intensity on sample history was observed at any temperature above T_N. At $T = 25$, 30, and 35 K, the magnetic diffuse scattering is dominated by a broad peak, which decreases in intensity and shifts from $q = 0.8$ to 0.7 Å^{-1} with increasing temperature. At $T \geqslant 50$ K, the scattering patterns show no pronounced features in the q range probed, but even at 100 K there are small differences between the experimental data and the paramagnetic Co^{3+} form factor which would be observed for entirely random spin orientations. We use two approaches to analyze the high-temperature data. First, we fit the data using reverse Monte Carlo refinement: this approach determines the paramagnetic correlations but does not model the magnetic interactions. Second, we consider the extent to which our data are consistent with different sets of interactions in a simple magnetic Hamiltonian. Throughout, we assume that only the Co^{3+}_{II} ($S = 2$) sites are magnetic with no magnetic moment present on the Co^{3+}_{I} ($S = 0$) sites (in agreement with NMR evidence [34]), and find that this assumption is entirely consistent with the data.

We performed RMC refinements of the high-temperature data using the SPINVERT program [28]. Technical details of the refinements were given in Sec. II. The most important assumption is that the spins behave as purely Ising variables, which is expected to be valid for $T \ll DS^2$. Measurements of the magnetic heat capacity [20] and our own analysis in Sec. IV suggest that the Ising approximation is valid at least for $T \lesssim 50$ K, where the diffuse scattering shows the most pronounced features. We make the usual assumption that the magnetic form factor is given by the dipole (low-q) formula $f(q) = j_0(q) + C_2 j_2(q)$, where $j_0(q)$ and $j_2(q)$ are tabulated functions [35]

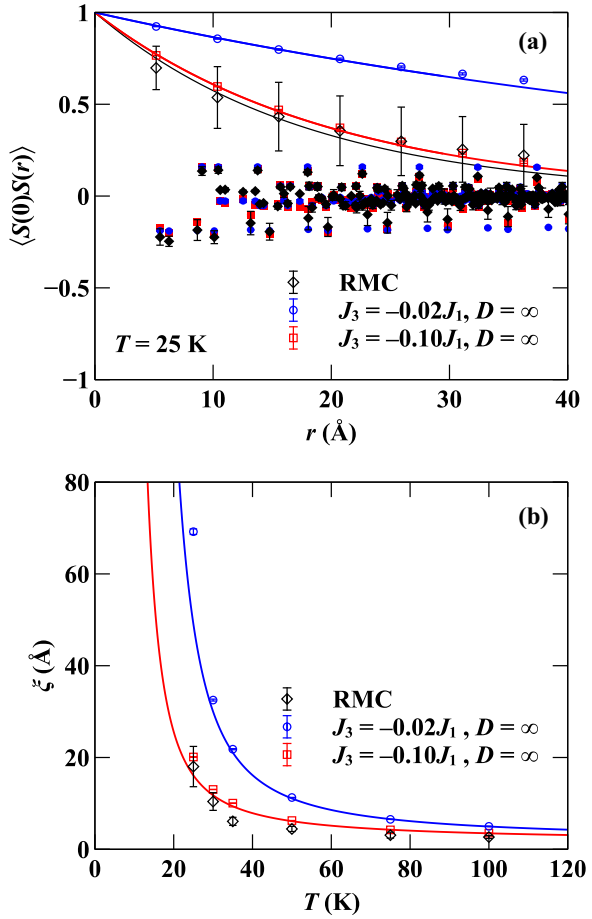

FIG. 4. (Color online) (a) Radial spin correlation function at $T = 25$ K. Results from reverse Monte Carlo fits to the $T = 25$ K data are shown in black. Values from the direct Monte Carlo simulations with $J_3/J_1 = -0.10$ ($J_1S^2 = 22.9$ K) and $J_3/J_1 = -0.02$ ($J_1S^2 = 36.8$ K) are colored red and blue, respectively. Correlations within the Ising chains (intrachain correlations) are shown as open symbols and correlations between different Ising chains (interchain correlations) are shown as closed symbols. (b) Temperature evolution of the ferromagnetic intrachain correlation length ξ (colors as above). The solid lines show the exact expression [Eq. (7) in the text] for independent ferromagnetic Ising chains for $J_1S^2 = 22.9$ K (red line) and $J_1S^2 = 36.8$ K (blue line).

and the factor $C_2 = L^z/(2S^z + L^z)$ accounts for the orbital contribution to the magnetic moment; we take $C_2 = 0.25$ as an average of the literature values for $Ca_3Co_2O_6$ [1,2,5,36]. All fits are modified by an overall intensity scale factor in order to match the data. The optimal value of the scale factor was obtained by fitting the 25-K data and then fixed at this value when fitting the higher-temperature data sets. The fits we obtain are shown in Fig. 3, and represent excellent agreement with the data.

The radial spin correlation function $\langle S(0)S(r)\rangle$ obtained from RMC refinement of the 25-K data is shown in Fig. 4(a). Correlations along the Ising spin chains $\langle S(0)S(r_z)\rangle$ are FM and decay with distance r_z along the chains. This distance dependence can be fitted by an exponential decay $\langle S(0)S(r_z)\rangle = \exp(-r_z/\xi)$, in agreement with the theoretical calculation for the one-dimensional (1D) FM Ising model (i.e., independent chains) [37]. By contrast, correlations between different chains are AFM, of smaller magnitude than the intrachain correlations, and are not well described by an exponential decay; we consider them in more detail below. The temperature dependence of the FM correlation length ξ is shown in Fig. 4(b). The values shown were determined by fitting $\langle S(0)S(r_z)\rangle$ with an exponential for each of the six measured temperatures. The fitting range was $0 < r < 30$ Å (except at 100 K where the upper limit was reduced to $r = 20$ Å due to the rapid decay of the correlations); in all cases, the quality of the fit was similar to that obtained at 25 K. The value of ξ falls rapidly with increasing temperature just above T_N, but decreases more slowly at higher temperatures. Here again we note a similarity with the theoretical expression for the 1D Ising model [37]

$$\xi = \frac{c}{2\ln[\coth(J_1S^2/T)]}, \tag{7}$$

where $c = 10.367$ Å, which also has a "long tail" at high temperature.

We note two qualifications regarding the RMC refinements. First, since RMC refinement is a stochastic process, the values of ξ obtained from RMC represent lower bounds on the true values. Second, we found that making small changes to refinement parameters (in particular the intensity scale) resulted in significant variations in the absolute values obtained for the FM correlation length. In order to estimate the uncertainties shown in Fig. 4 for $\langle S(0)S(r)\rangle$ and ξ, we therefore considered the effect of changing the scale by a small amount δs from its refined value s, where $\delta s = 0.1s$ was chosen as the range over which it was possible to obtain reasonable fits to the data.

We now consider the extent to which the magnetic diffuse scattering data above T_N can be modeled using a magnetic Hamiltonian. Following previous work [15], we consider a model of Ising spins coupled by interactions between nearest neighbors (J_1 at 5.18 Å), next-nearest neighbors (J_2 at 5.51 Å), and third neighbors (J_3 at 6.23 Å). Our initial calculations revealed that the 25-K data can be well described by at least two different sets of parameters: either J_1 and J_3 (with $J_2 = 0$), or J_1 and J_2 (with $J_3 = 0$). An independent determination of both J_2 and J_3 is therefore not possible using only the diffuse scattering data. However, it has been argued that J_3 should be of significantly greater magnitude than J_2, based on the shorter O–O bond distance for the J_3 pathway [14] and on spin-dimer calculations [15]. We therefore assume initially that $J_2 = 0$ and attempt to determine the values of only J_1 and J_3. These interaction pathways are shown in Fig. 5. To this end, we performed direct Monte Carlo (DMC) simulations of the Ising Hamiltonian [Eq. (2)] as described in Sec. II. For each ratio of J_3/J_1 that we considered, we determined the ratio T/J_1S^2 for which the calculated $I(q)$ most closely matched the 25-K data. This procedure fixes the absolute value of J_1 and hence allows model and experimental data to be compared for each of the measured temperatures. The values of J_3 obtained in this way can probably be interpreted as an overall AFM exchange interaction $J_2 + J_3$, since our simulations of the paramagnetic phase are insensitive to whether the AFM coupling is J_2, J_3, or a combination of both.

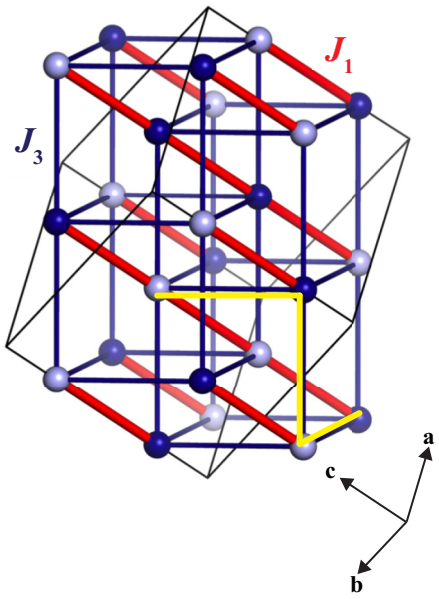

FIG. 5. (Color online) Magnetic interaction pathways in $Ca_3Co_2O_6$ (only $Co^{3+}_{II}, S = 2$ are shown). Ferromagnetic intrachain couplings J_1 are shown as red lines and antiferromagnetic (AFM) interchain couplings J_3 are shown as blue lines [38]. Light and dark blue circles indicate the long-range magnetic ordering which would be obtained in the hypothetical case that $J_1 = 0$ with AFM J_3. Yellow lines show the shortest path between two sites within the same Ising chain if only J_3 pathways are used.

Results of our simulations are shown in Figs. 3 and 4. We present results for $J_3/J_1 = -0.02$, which is the ratio suggested in Ref. [15], and for $J_3/J_1 = -0.10$, for comparison with our analysis of thermodynamic data in Sec. IV. At most temperatures, both sets of interactions show good agreement with the data. There is a slight tendency for all the model calculations to lie below the data at low q and above the data at high q, which may indicate a small inaccuracy in the assumed magnetic form factor. The $J_3/J_1 = -0.02$ model appears to fit the data better at 25 K, but the $J_3/J_1 = -0.10$ model is more successful at reproducing the shape of the main peak at 35 K (Fig. 3). The spin correlations for both models are shown in Fig. 4 and demonstrate the same qualitative features as the RMC results. The largest difference between the two models occurs in the region $q \lesssim 0.5$ Å^{-1}, with smaller values of $|J_3/J_1|$ associated with increased scattering intensity as $q \to 0$. Figure 4(b) shows that this increased intensity at low q is associated with a larger value of the FM correlation length ξ. Unfortunately, since the low-q region is not accessed experimentally, the diffraction data are relatively insensitive to the values of ξ and J_3/J_1. In order to place a stronger restriction on J_3/J_1, it is necessary to consider thermodynamic data together with diffraction, an approach we will follow in Sec. IV.

Despite these limitations, it is possible to draw some general conclusions about the intrachain correlations from Fig. 4(b). Most significant is that, for the values of J_3/J_1 considered here, the values of ξ from DMC simulation agree with the exact result for independent FM Ising chains [Eq. (7)] with no fitting parameters. This result suggests that the FM correlations are strongly 1D above T_N. Hence, the J_3 interaction, which couples intrachain spins by the indirect pathway shown in Fig. 5, has a negligible effect on the intrachain correlations for small $|J_3/J_1| \lesssim 0.10$. A small J_3/J_1 ratio is a prerequisite both for 1D behavior and frustration since in the opposite limit $|J_3/J_1| \gg 1$ the conventional three-dimensional order shown in Fig. 5 would occur. Further evidence for 1D behavior comes from the correlation strength. At the nearest-neighbor distance, we obtain $0.1 \lesssim \langle S(0)S(c/2)\rangle \lesssim 0.35$ at 100 K (lower bounds are RMC results and upper bounds are for $J_3/J_1 = -0.02$); although small in absolute terms, these values are at least double the result for a three-dimensional Ising model at $T \approx 4T_c$ [39]. Mindful that our assumption of Ising spins may be less accurate for $T \gtrsim 50$ K, we also considered a Heisenberg model with $J_3/J_1 = -0.10$ and finite single-ion anisotropy $D/J_1 = 32$ (discussed further in Sec. IV), which showed the same behavior except for slightly reduced correlation lengths at high T (ξ around 90% of the Ising result at $T = 100$ K). The presence of 1D FM correlations well above T_N has been inferred (although not modeled) using other experimental techniques: Mössbauer studies on ^{159}Eu-doped $Ca_3Co_2O_6$ indicate a progressive increase in linewidth below $T \approx 150$ K [40]; μSR data indicate exponential-like relaxation to $T \approx 150$ K [41]; and inelastic neutron scattering (INS) measurements show that dispersive magnetic excitations persist to $T \approx 150$ K [4].

We now turn to the interchain correlations, which we probe by calculating the Fourier transform of the spin correlation function in the $(hk0)$ plane. This quantity $I(\mathbf{q})$ is of topical interest because it can be measured by neutron diffraction on a suitable arrangement of single crystals, which has recently been reported for $Ca_3Co_2O_6$ [4]. In Fig. 6, we show the calculated $I(\mathbf{q})$ in the $(hk0)$ reciprocal space plane for three models of $Ca_3Co_2O_6$ at $T = 25$ K: the DMC model with $J_3/J_1 = -0.10$ in Fig. 6(a); the DMC model with $J_3/J_1 = -0.02$ in Fig. 6(b); and the RMC model obtained from fitting the powder data in Fig. 6(c). In each case, the magnetic diffuse

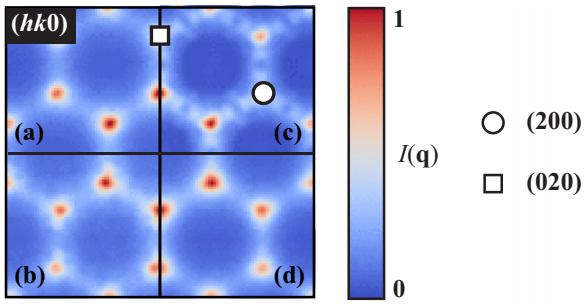

FIG. 6. (Color online) Calculated single-crystal diffuse scattering patterns at $T = 25$ K for models of $Ca_3Co_2O_6$ discussed in the text: (a) direct Monte Carlo, $J_3/J_1 = -0.10$ ($J_1S^2 = 22.9$ K); (b) direct Monte Carlo, $J_3/J_1 = -0.02$ ($J_1S^2 = 36.8$ K); (c) reverse Monte Carlo, from fitting $T = 25$ K powder data; (d) Wannier model of Ising spins on the triangular lattice calculated using Monte Carlo simulation at $T = 1.5|J|$, where J is the nearest-neighbor AFM interaction. All panels show the $(hk0)$ reciprocal-space plane. The intensity scales are chosen so that the most intense feature in each panel is normalized to 1.

scattering pattern was calculated from the spin configurations using the general equation [42]

$$I(\mathbf{q}) = [f(q)]^2 \sum_{i,j} \mathbf{S}_i^{\perp} \cdot \mathbf{S}_j^{\perp} \exp[i\mathbf{q} \cdot (\mathbf{r}_i - \mathbf{r}_j)], \qquad (8)$$

where $f(q)$ is the Co^{3+} magnetic form factor [35], $\mathbf{q}$ is the scattering vector, and $\mathbf{S}_i^{\perp}$ is the spin vector located at $\mathbf{r}_i$, projected perpendicular to $\mathbf{q}$. The sum is taken over all pairs of spins separated by distances $|\mathbf{r}_i - \mathbf{r}_j| \lesssim 45$ Å. In all cases, the diffuse scattering takes the form of triangle-shaped peaks at the corners of the second Brillouin zone. The fact that similar results are obtained from both RMC refinement and a physically sensible set of magnetic interactions suggests that our prediction of $I(\mathbf{q})$ is robust. Our calculations also indicate that a single-crystal neutron-scattering measurement of the $(hk0)$ plane would provide rather little information on the relative strength of FM and AFM interactions. Instead, it would probably be necessary to measure one of the diffuse peaks along $\mathbf{c}^*$ in order to obtain the FM correlation length as a function of temperature. Finally, in Fig. 6(d) we show the calculated $I(\mathbf{q})$ for the nearest-neighbor Ising antiferromagnet on the triangular lattice [43] (henceforth "Wannier model") which has previously been applied in several theoretical studies of $Ca_3Co_2O_6$ (see, e.g., Refs. [6–8]). We find close agreement between Figs. 6(a)–6(c) and the Wannier model for $T \sim |J|$ (the calculation shown is for $T = 1.5|J|$). The extent of this agreement is rather surprising since the modulation of the diffuse scattering is sensitive to small changes in the magnetic interactions [44]. Hence, although the Wannier model can provide no information on the intrachain correlations, it seems to provide a good qualitative description of the interchain spin correlations.

In summary, our results indicate a physical picture of paramagnetic $Ca_3Co_2O_6$ in which weak interchain correlations resemble the Wannier model, and the length scale ξ over which these correlations remain coherent along the c axis can be calculated as if the chains behave independently. In this sense, above T_N, the correlations along c are effectively decoupled from those in the ab plane.

IV. MODELING OF BULK PROPERTIES

In this section, we employ direct Monte Carlo simulations to calculate bulk properties of $Ca_3Co_2O_6$ in the paramagnetic phase. Our motivation for considering bulk properties is the strong dependence of the limiting value $I(q \to 0)$ on the ratio J_3/J_1, which suggests that the bulk susceptibility is sensitive to the strength of both FM and AFM interactions. Here, Monte Carlo simulation has two important advantages over traditional approaches to fitting the susceptibility [2,13,45,46]: first, it is not limited by the number or type of interactions which can be modeled; second, it is not restricted to the high-temperature limit, remaining accurate until the correlation length becomes of the order of the simulation size.

In Fig. 7(a), the product of the magnetic susceptibility per spin and temperature χT is shown for different values of J_3/J_1. The susceptibility is calculated parallel to the direction of the chains (i.e., along c) as described in Sec. II. The results show two main features. First, there is an anomaly at the Néel temperature $T_N \sim J_1 S^2$. The value of T_N decreases with

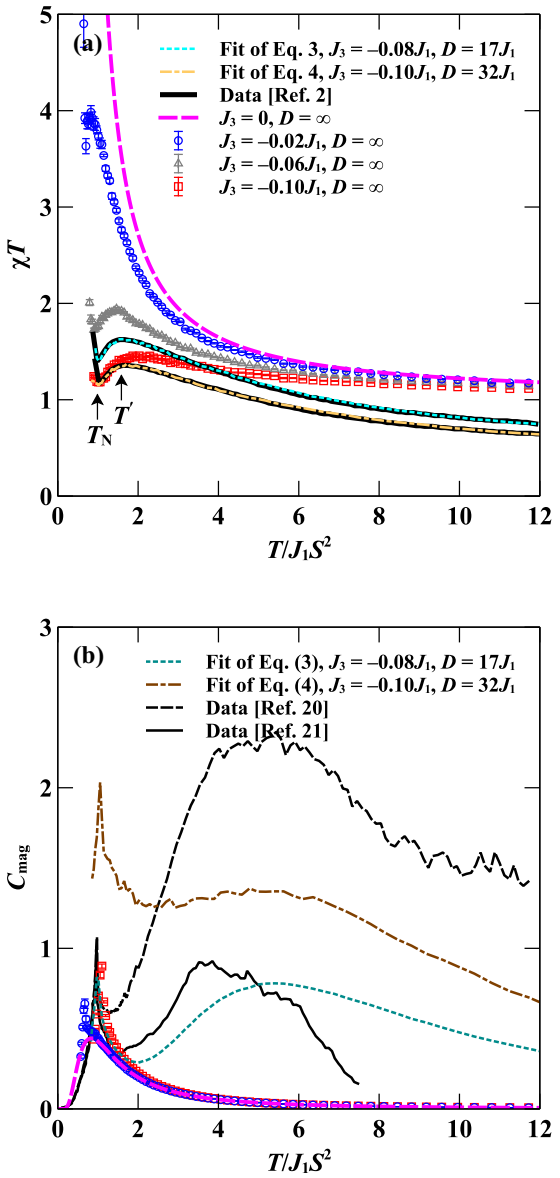

FIG. 7. (Color online) (a) Magnetic susceptibility per spin of $Ca_3Co_2O_6$ parallel to the Ising chains. Results from DMC simulations are shown for the Ising model with $J_3/J_1 = -0.02$ (blue circles); $J_3/J_1 = -0.06$ (gray triangles); $J_3/J_1 = -0.10$ (red squares), five-state model with $J_3/J_1 = -0.08$ and $D/J_1 = 17$ (cyan dotted line), and anisotropic Heisenberg model with $J_3/J_1 = -0.10$ and $D/J_1 = 32$ (brown dotted-dashed line). The exact result [37] for FM J_1 only, $\chi T = \exp(2J_1S^2/T)$, is shown for comparison (dashed magenta line). Experimental data (from Ref. [2]) are shown as solid black lines, and have been scaled to match the fits for the anisotropic models. (b) Magnetic heat capacity per spin of $Ca_3Co_2O_6$. Results from DMC simulations have the same symbols as in (a). The exact result [37] for FM J_1 only, $C_{mag} = (J_1S^2/T)^2/\cosh^2(J_1S^2/T)$, is shown as a dashed magenta line. Data from Refs. [20,21] are shown as dashed and solid black lines, respectively.

decreasing $|J_3/J_1|$, as one expects, since $T_N = 0$ in the limit of independent chains [37]. (We note that a value $T_N = 0$ can not be obtained in Monte Carlo simulation due to the finite simulation size; for a model with only FM J_1 interactions,

ξ approaches the size of our simulation at $T \approx 0.4 J_1 S^2$, which is significantly below the transition temperatures we observe for the J_1-J_3 model.) Second, there is a broad peak at $T' > T_N$, which sharpens and moves closer to T_N as $|J_3/J_1|$ is decreased. In this respect, our simulations reproduce experimental measurements of the parallel susceptibility, which also show a broad peak at $T' \approx 40$ K ($= 1.6 T_N$) [2,19]. From Fig. 7(a), the experimental location of T' implies that $0.06 \lesssim |J_3/J_1| \lesssim 0.10$. Our results show that the T' peak arises from the development of AFM interchain correlations since the diffraction measurements show the development of an AFM peak close to T' (Fig. 3), while the intrachain correlations remain FM throughout the measured temperature range [Fig. 4(b)].

Although simulations of the Ising model show qualitative agreement with the experimental data for $T \gtrsim T_N$, it proved impossible to obtain a satisfactory fit overall: the problem is that the gradient of the Ising curve is too shallow at higher temperatures [Fig. 7(a)]. This is a likely consequence of the failure of the Ising approximation for $T \gtrsim 50$ K. To quantify the effect of finite D in addition to J_3, we considered the two candidate anisotropic models introduced in Sec. II: the five-state model [Eq. (3)] and the anisotropic Heisenberg model [Eq. (4)]. For each model, we used a grid search to fit the values of J_3 and D to the experimental susceptibility data of Ref. [2] for $T > T_N$. (We note that the susceptibility data of Ref. [2] agree with Ref. [46] and with data collected on powder samples, but do not appear to correspond to the data of Ref. [19] at higher temperatures; the reason for this discrepancy is unclear at present.) For a given set of interaction parameters, the calculated curve was first normalized horizontally by the position of T_N and a linear least-squares fit was then performed to determine the vertical scale factor. The success of this procedure relies on the fact that J_3 and D are weakly correlated since the effect of J_3 is most important just above T_N, whereas the effect of finite D is evident at high temperature.

Fits of the two anisotropic models are shown in Fig. 7(a). In both cases, quantitative agreement with the data is obtained throughout the paramagnetic regime. The fitted values of J_1, J_3, and D are given in Table I, where we have placed the interaction parameters on an absolute scale using the value of T_N/JS^2, taking $S = 2$. We note that (by convention) the orbital contribution to the magnetic moment is not included here, even though it represents a significant fraction of the total moment in $Ca_3Co_2O_6$ [36]. The fitted values of the exchange constants $J_1 \approx 6$ K and $J_3 \approx -0.6$ K are nearly consistent for both anisotropic models, but the value of D shows a significant model dependence (Table I). This difference is perhaps not unexpected given that D has a different meaning in the two models. We also obtain the length of the effective magnetic moment μ_{eff} from the vertical scale factor using the relation $(\chi T)_{\text{expt}} = 0.375(\mu_{\text{eff}}/\mu_B)^2 (\chi T)_{\text{MC}}$, where $(\chi T)_{\text{expt}}$ is given in K emu mol^{-1}. The fitted values are given in Table I and are consistent with theoretical studies ($\sim 5.7 \mu_B$) [5], magnetization measurements ($\sim 4.8 \mu_B$) [2], and an x-ray circular dichroism study ($\sim 5.3 \mu_B$) [36].

TABLE I. Values of magnetic exchange interactions J_1 and J_3, single-ion anisotropy D, and effective magnetic moment μ_{eff} obtained by fitting the experimental magnetic susceptibility data of Ref. [2]. The two models fitted are the five-state model [Eq. (3)] and the anisotropic Heisenberg model [Eq. (4)]. Conservative error bars were estimated from two points adjacent to the best-fit point on our grid ($\delta J_3 = 0.1 J_1$, $\delta D \approx 3 J_1$).

Parameter	Fit of Eq. (3), $J_3 = -0.08 J_1$, $D = 17 J_1$	Fit of Eq. (4) $J_3 = -0.10 J_1$, $D = 32 J_1$
J_1 (K)	6.3 ± 0.3	6.0 ± 0.2
J_3 (K)	−0.50 ± 0.04	−0.60 ± 0.04
D (K)	190 ± 30	110 ± 20
μ_{eff}/μ_B	4.8 ± 0.2	5.3 ± 0.2

Since considering a finite anisotropy term introduces an extra parameter compared to an Ising model, it is important to ask whether this explains any measurements beyond the susceptibility. One such measurement is the magnetic heat capacity C_{mag}. In addition to the expected peak at T_N, the experimental C_{mag} shows a broad high-T peak between 80 and 160 K [20,21]. Although the presence of this peak is not in doubt, its intensity is quite uncertain due to the effect of the lattice subtraction, as a comparison of data from Refs. [20,21] shows [Fig. 7(b)]. In Ref. [21], the high-T peak was ascribed to the development of short-range intrachain correlations, which release all the entropy in a fully 1D model. If this explanation is correct, then the large separation between the high-T peak and T_N would suggest that $Ca_3Co_2O_6$ has much more 1D character than the canonical Ising spin-chain compound $CoCl_2 \cdot 2NC_5H_5$, for which the high-T peak is nearly obscured by the T_N peak [47]. In Fig. 7(b), we plot the magnetic heat capacity from DMC simulations of the Ising model for $J_3/J_1 = -0.10$ and $J_3/J_1 = -0.02$. For $J_3/J_1 = -0.10$, the high-T peak is obscured by the T_N peak, and even for $J_3/J_1 = -0.02$ it is only just visible as a shoulder on the T_N peak. Therefore, an Ising model can only explain the existence of the high-T peak if $|J_3/J_1| \ll 0.02$. We now consider the two anisotropic models with the interaction parameters given in Table I. The five-state model shows a broad peak at $T \approx 140$ K ($=1.3D$), in qualitative agreement with the experimental data [Fig. 7(b)]. This agreement provides strong evidence that the high-T peak is actually a magnetic Schottky anomaly resulting from the temperature-dependent population of the S^z states. Our results are supported by quantum calculations of the anisotropic $S = 2$ Heisenberg chain, which predict an extra peak in C_{mag} at $T = 1.4D$ for large but finite D [48]. For completeness, we also show the anisotropic Heisenberg C_{mag} curve in Fig. 7(b). The less satisfactory agreement with the data is due to the failure of the vector-spin approximation of Eq. (4), which permits magnetic excitations which cost an infinitesimal amount of energy and leads to a diverging value of the magnetic entropy [49]. By contrast, the five-state model has the correct value of the entropy for $S = 2$ spins ($\ln 5$ per spin) in the high-temperature limit.

We now present a brief comparison of our values for J_1, J_3, and D with literature results. Values of these parameters have been reported separately, although a simultaneous fit of all three parameters has not been performed before. In Ref. [2], a fit to the single-crystal magnetic susceptibility yielded $J_1 =$ 13 K; the disagreement with our results is probably due to

the assumption of an Ising model up to room temperature. We find better agreement with the results of Ref. [46], in which the susceptibility was fitted to a model including both J_1 and D. Recently reported INS measurements [4] show a weakly dispersive spin wave propagating along $\mathbf{c}^*$ with a large spin gap $\omega_0 \approx 27$ meV ($= 310$ K). The dispersion was fitted using linear spin-wave theory to obtain (for isotropic exchange) $J_1 = 4.9$ K and $D = \omega_0/2S = 79$ K (the resolution of the data did not allow J_3 to be determined). We note that taking into account higher-order corrections to the spin-wave theory leads to a modified equation for the spin gap $D = \omega_0/(2S-1)$ [48], which would yield $D = 105$ K for the data of Ref. [4]. These results are in reasonable agreement ($\sim 20\%$) with our five-state model. Very recently, values of the exchange interactions were obtained using ^{59}Co NMR to determine the energy cost of spin flips in the SDW phase, yielding (in our notation) $J_1 = 6.0$ K and $J_2 + J_3 = -0.58$ K. The good agreement with our results is striking given the entirely different experimental technique and modeling approach considered in Ref. [50].

Finally, we consider our results in the context of the magnetic ordering identified by neutron diffraction. The first ordered state that develops at T_N is a SDW with an incommensurate magnetic propagation vector $\mathbf{k} \approx (0,0,1.01)$ [16,17]. Within a mean-field theory, this propagation vector would require that $J_3/J_1 = -0.02$ if J_2 is negligibly small [15]. The ratio $J_3/J_1 \approx -0.10$ we have determined would produce a shorter-wavelength modulation with $\mathbf{k} \approx (0,0,1.05)$. However, as Fig. 7(a) shows, choosing $J_3/J_1 = -0.02$ to agree with Ref. [15] gives a much less successful description of the experimental susceptibility data. This discrepancy may be a consequence of the assumptions of Ref. [15], which considered a mean-field model without magnetic anisotropy. Alternatively, J_2 may not actually be negligible compared to J_3, which has recently been proposed in the analysis of NMR data [50]. By choosing J_2 and J_3 appropriately, both the overall energy of AFM interactions and the experimental propagation vector can be reproduced. For $J_2 + J_3 = -0.10J_1$, this occurs when $J_2 = J_3 = -0.05J_1$ [15]. We have checked that these values yield a χT curve which is qualitatively close to the one shown previously for $J_3/J_1 = -0.10$ ($J_2 = 0$). To the best of our knowledge, a practical experimental method to determine J_2 and J_3 independently has not yet been identified, and this remains a challenge for future work.

V. CONCLUSIONS

In summary, polarized neutron diffraction measurements performed on $Ca_3Co_2O_6$ give clear evidence of the coexistence of the two different magnetic structures in this compound below T_N: a spin-density wave structure and a commensurate antiferromagnetic structure. The volume fraction of the phases is dependent on sample history in general, and on cooling rates in particular, with slow cooling rates providing easier access to the commensurate antiferromagnetic phase. Given that relatively little is known about the behavior of the CAFM phase in an applied field [3] and that for the SDW phase the magnetic states for a zero-field-cooled sample and a sample that has previously been exposed to a high magnetic field are completely different on a microscopic level [51], it would be extremely interesting to extend the neutron scattering measurements to an applied field. Ideally, such an experiment should be performed on an arrangement of single crystals with appreciable volume, which has recently been reported [4].

Above T_N, we performed reverse Monte Carlo refinements and direct Monte Carlo simulations to model the magnetic diffuse scattering data. Our results show that intrachain spin correlations remain ferromagnetic at all temperatures, decay approximately exponentially with distance along the chain, and exhibit a temperature-dependent correlation length which is well described by the one-dimensional Ising model over the temperature range studied ($T_N \lesssim T \lesssim 100$ K). Interchain correlations are weaker and antiferromagnetic, and have a diffraction pattern showing strong qualitative similarities to the nearest-neighbor antiferromagnet on the triangular lattice for $T \sim |J|$. Perhaps our most intriguing result is that important aspects of these two canonical models are simultaneously realized in paramagnetic $Ca_3Co_2O_6$, i.e., intrachain and interchain correlations are essentially decoupled. This conclusion could be tested further by performing single-crystal neutron diffraction experiments to measure the magnetic diffuse scattering above T_N.

Finally, we have fitted published measurements of the single-crystal magnetic susceptibility to obtain the exchange constants J_1 and J_3 (assuming $J_2 = 0$) and the single-ion anisotropy D. Surprisingly, bulk susceptibility data are more sensitive than the magnetic diffuse scattering data to the values of J_3 and D in this system. For a five-state model, we obtain $J_1 \approx 6$ K, $J_3 \approx -0.6$ K, and $D \approx 110$ K (noting, however, that the value of D is dependent on the assumed form of the classical Hamiltonian). These values explain two anomalies in bulk measurements: (i) the high-temperature susceptibility peak at $T' \approx 40$ K, and (ii) the broad maximum in magnetic specific heat at $T \sim 100$ K, which we interpret as a magnetic Schottky anomaly. This three-parameter model is the first to explain the temperature dependence of bulk measurements in $Ca_3Co_2O_6$ between T_N and room temperature, and should therefore provide a useful starting point for quantitative modeling of the magnetic behavior of $Ca_3Co_2O_6$ as a function of temperature and applied magnetic field.

ACKNOWLEDGMENTS

We are grateful to M. J. Cliffe, L. C. Chapon, and P. Manuel for valuable discussions. J.A.M.P. and A.L.G. gratefully acknowledge financial support from the STFC, EPSRC (Grant No. EP/G004528/2) and ERC (Ref No.: 279705).

[1] V. Hardy, M. R. Lees, O. A. Petrenko, D. McK. Paul, D. Flahaut, S. Hébert, and A. Maignan, Phys. Rev. B **70**, 064424 (2004).

[2] A. Maignan *et al.*, J. Mater. Chem. **14**, 1231 (2004).

[3] S. Agrestini, C. L. Fleck, L. C. Chapon, C. Mazzoli, A. Bombardi, M. R. Lees, and O. A. Petrenko, Phys. Rev. Lett. **106**, 197204 (2011).

[4] A. Jain, P. Y. Portnichenko, H. Jang, G. Jackeli, G. Friemel, A. Ivanov, A. Piovano, S. M. Yusuf, B. Keimer, and D. S. Inosov, Phys. Rev. B **88**, 224403 (2013).

[5] H. Wu, M. W. Haverkort, Z. Hu, D. I. Khomskii, and L. H. Tjeng, Phys. Rev. Lett. **95**, 186401 (2005).

[6] Y. B. Kudasov, Phys. Rev. Lett. **96**, 027212 (2006).

[7] Y. B. Kudasov, Europhys. Lett. **78**, 57005 (2007).

[8] X. Yao, S. Dong, H. Yu, and J. Liu, Phys. Rev. B **74**, 134421 (2006).

[9] Y. Kamiya and C. D. Batista, Phys. Rev. Lett. **109**, 067204 (2012).

[10] Y. B. Kudasov, A. S. Korshunov, V. N. Pavlov, and D. A. Maslov, Phys.-Usp. **55**, 1169 (2012).

[11] H. Fjellvåg, E. Gulbrandsen, S. Aasland, A. Olsen, and B. C. Hauback, J. Solid State Chem. **124**, 190 (1996).

[12] K. Takubo, T. Mizokawa, S. Hirata, J.-Y. Son, A. Fujimori, D. Topwal, D. D. Sarma, S. Rayaprol, and E.-V. Sampathkumaran, Phys. Rev. B **71**, 073406 (2005).

[13] H. Kageyama *et al.*, J. Phys. Soc. Jpn. **66**, 3996 (1997).

[14] R. Frésard, C. Laschinger, T. Kopp, and V. Eyert, Phys. Rev. B **69**, 140405 (2004).

[15] L. C. Chapon, Phys. Rev. B **80**, 172405 (2009).

[16] S. Agrestini, L. C. Chapon, A. Daoud-Aladine, J. Schefer, A. Gukasov, C. Mazzoli, M. R. Lees, and O. A. Petrenko, Phys. Rev. Lett. **101**, 097207 (2008).

[17] S. Agrestini, C. Mazzoli, A. Bombardi, and M. R. Lees, Phys. Rev. B **77**, 140403 (2008).

[18] T. Moyoshi and K. Motoya, J. Phys. Soc. Jpn. **80**, 034701 (2011).

[19] J.-G. Cheng, J.-S. Zhou, and J. B. Goodenough, Phys. Rev. B **79**, 184414 (2009).

[20] V. Hardy *et al.*, J. Phys.: Condens. Matter **15**, 5737 (2003).

[21] V. Hardy, S. Lambert, M. R. Lees, and D. McK. Paul, Phys. Rev. B **68**, 014424 (2003).

[22] H. Kageyama, K. Yoshimura, K. Kosuge, H. Mitamura, and T. Goto, J. Phys. Soc. Jpn. **66**, 1607 (1997).

[23] A. Maignan, C. Michel, A. C. Masset, C. Martin, and B. Raveau, Eur. Phys. J. B **15**, 657 (2000).

[24] V. Hardy, D. Flahaut, M. R. Lees, and O. A. Petrenko, Phys. Rev. B **70**, 214439 (2004).

[25] J. R. Stewart *et al.*, J. Appl. Crystallogr. **42**, 69 (2009).

[26] G. Ehlers, J. R. Stewart, A. R. Wildes, P. P. Deen, and K. H. Andersen, Rev. Sci. Instrum. **84**, 093901 (2013).

[27] J. Rodríguez-Carvajal, Physica B **192**, 55 (1993).

[28] J. A. M. Paddison, J. R. Stewart, and A. L. Goodwin, J. Phys.: Condens. Matter **25**, 454220 (2013).

[29] R. L. McGreevy and L. Pusztai, Mol. Simul. **1**, 359 (1988).

[30] J. A. M. Paddison and A. L. Goodwin, Phys. Rev. Lett. **108**, 017204 (2012).

[31] I. A. Blech and B. L. Averbach, Physics **1**, 31 (1964).

[32] D. Hinzke and U. Nowak, Comput. Phys. Commun. **121–122**, 334 (1999).

[33] P. Lampen, N. S. Bingham, M. H. Phan, H. Srikanth, H. T. Yi, and S. W. Cheong, Phys. Rev. B **89**, 144414 (2014).

[34] G. Allodi, R. De Renzi, S. Agrestini, C. Mazzoli, and M. R. Lees, Phys. Rev. B **83**, 104408 (2011).

[35] P. J. Brown, *International Tables for Crystallography Vol. C* (Kluwer-Academic, Amsterdam, 2004), pp. 454–460.

[36] T. Burnus *et al.*, Phys. Rev. B **74**, 245111 (2006).

[37] R. J. Baxter, *Exactly Solved Models in Statistical Mechanics* (Academic, New York, 1982).

[38] The orthorhombic axes are related to the hexagonal axes by $\mathbf{a}_o = \mathbf{a}_h$, $\mathbf{b}_o = \mathbf{a}_h + 2\mathbf{b}_h$, $\mathbf{c}_o = \mathbf{c}_h$.

[39] H. Müller-Krumbhaar and K. Binder, J. Stat. Phys. **8**, 1 (1973).

[40] P. L. Paulose, N. Mohapatra, and E. V. Sampathkumaran, Phys. Rev. B **77**, 172403 (2008).

[41] S. Takeshita, J. Arai, T. Goko, K. Nishiyama, and K. Nagamine, J. Phys. Soc. Jpn. **75**, 034712 (2006).

[42] G. L. Squires, *Introduction to the Theory of Thermal Neutron Scattering* (Cambridge University Press, Cambridge, UK, 1978).

[43] G. H. Wannier, Phys. Rev. **79**, 357 (1950).

[44] T. R. Welberry, A. P. Heerdegen, D. C. Goldstone, and I. A. Taylor, Acta Crystallogr., Sect. B: Struct. Sci. **67**, 516 (2011).

[45] B. Martínez, V. Laukhin, M. Hernando, J. Fontcuberta, M. Parras, and J. M. González-Calbet, Phys. Rev. B **64**, 012417 (2001).

[46] V. Hardy, D. Flahaut, R. Frésard, and A. Maignan, J. Phys.: Condens. Matter **19**, 145229 (2007).

[47] K. Takeda, S. I. Matsukawa, and T. Haseda, J. Phys. Soc. Jpn. **30**, 1330 (1971).

[48] I. J. Junger, D. Ihle, and J. Richter, Phys. Rev. B **72**, 064454 (2005).

[49] M. E. Fisher, Am. J. Phys. **32**, 343 (1964).

[50] G. Allodi, P. Santini, S. Carretta, S. Agrestini, C. Mazzoli, A. Bombardi, M. R. Lees, and R. De Renzi, Phys. Rev. B **89**, 104401 (2014).

[51] C. L. Fleck, M. R. Lees, S. Agrestini, G. J. McIntyre, and O. A. Petrenko, EPL **90**, 67006 (2010).